

Available online at www.sciencedirect.com

jmr&t
Journal of Materials Research and Technology
journal homepage: www.elsevier.com/locate/jmrt



Ti–Mo–Zr alloys for bone repair: mechanical properties, corrosion resistance, and biological performance

Zhijun Guo ^{a,b,1}, Yizhou Huang ^{c,1}, Chunchun Sun ^b, Zengxing He ^d,
Delin Yuan ^b, Bianyun Cai ^e, Yunfeng Li ^{d,*}, Baolong Shen ^{a,**}

^a School of Materials Science and Engineering, Jiangsu Key Laboratory for Advanced Metallic Materials, Southeast University, Nanjing, 2111189, China

^b School of Materials and Physics, China University of Mining and Technology, Xuzhou, 221116, China

^c Department of Orthopedic Surgery and Orthopedic Research Institute, Laboratory of Stem Cell and Tissue Engineering, State Key Laboratory of Biotherapy, West China Hospital, Sichuan University, Chengdu, 610041, China

^d State Key Laboratory of Oral Diseases, National Clinical Research Center for Oral Diseases, West China Hospital of Stomatology, Sichuan University, Chengdu, 610041, China

^e College of Medical Technology and Engineering, Henan University of Science and Technology, Luoyang, 471023, China

ARTICLE INFO

Article history:

Received 1 January 2023

Accepted 1 May 2023

Available online 5 May 2023

Keywords:

Titanium

Molybdenum

Zirconium

Young's modulus

Osteointegration

Bone repair

ABSTRACT

Titanium (Ti) alloys have been widely used as bone implants, but challenges such as the stress shielding effect still compromise long-term clinical successes. To improve the mechanical properties of Ti, non-toxic alloying elements zirconium (Zr) and molybdenum (Mo) were added either alone or in combination to produce Ti–Mo–Zr alloys. The influence of Zr or Mo addition on the alloy properties, such as the microstructure and the corrosion resistance, were investigated. The cytocompatibility and osteointegration of prepared alloys were evaluated to determine the potential for bone repair. The results showed that Ti–10Zr displayed an acicular α' phase, while Ti–12Mo and Ti–12Mo–10Zr comprised a metastable β phase. Due to the solid solution and phase precipitation strengthening effect of Zr and Mo elements, the prepared alloys showed higher microhardness and compressive yield strength when compared with commercially pure Ti (CP–Ti). Ti–12Mo–10Zr possessed the lowest Young's modulus, while CP–Ti and Ti–10Zr showed a comparable Young's modulus. The corrosion resistance was in the order of Ti–12Mo–10Zr > Ti–12Mo > CP–Ti > Ti–10Zr. Notably, all alloys showed good cytocompatibility and osteointegration, which were similar to those of CP–Ti. Taken together, due to excellent material and biological performance, Ti–12Mo–10Zr presents a promising material for bone repair.

© 2023 The Authors. Published by Elsevier B.V. This is an open access article under the CC BY-NC-ND license (<http://creativecommons.org/licenses/by-nc-nd/4.0/>).

* Corresponding author.

** Corresponding author.

E-mail addresses: doctorlyf@163.com (Y. Li), blshen@seu.edu.cn (B. Shen).

¹ These authors contributed equally to this work as co-first authors.

<https://doi.org/10.1016/j.jmrt.2023.05.006>

2238-7854/© 2023 The Authors. Published by Elsevier B.V. This is an open access article under the CC BY-NC-ND license (<http://creativecommons.org/licenses/by-nc-nd/4.0/>).

Nomenclature

BIC	Bone-implant-contact
BV/TV	Bone volume/total sample volume
CCK-8	Cell counting kit-8
CPE	Constant phase element
CP-Ti	Commercially pure Ti
EDS	Energy dispersive spectroscopy
EIS	Electrochemical impedance spectroscopy
Mo	Molybdenum
OCP	Open circuit potential
OM	Optical microscopy
PBS	Phosphate buffer solution
SCE	Saturated calomel electrode
SEM	Scanning electron microscope
Tb·N	Trabecular number
Tb·Th	Trabecular thickness
Tb·Sp	Trabecular spacing
Ti	Titanium
VOI	Volume of interest
XPS	X-ray photoelectron spectroscopy
XRD	X-ray diffraction; Zr: Zirconium

1. Introduction

With an increasing aging population, the demand of metallic biomaterials to improve the life quality and longevity of patients is increasing [1]. Among traditional metal materials, titanium (Ti) alloys are common for bone implants owing to low density, high strength, and good biocompatibility [2]. In the clinic, most implants are expected to serve over 10 years. Although Ti alloys can provide the necessary mechanical support, several disadvantages usually lead to a short life span or even the failure of implants. Particularly, the Young's modulus of Ti is considerably higher than that of bone [3]. The biomechanical mismatch can cause a stress shielding effect that leads to bone absorption or atrophy. Another issue is that some traditional Ti alloys (e.g., Ti6Al4V) contain harmful elements (e.g., nickel, aluminum, and vanadium) that can lead to severe complications such as anemia and nerve disorders [4].

Several strategies have been developed to reduce the mechanical mismatch between Ti and bone, such as the fabrication of porous implants by additive manufacturing [5]. The advantages of porous 3D-printed Ti implants have been confirmed in animal studies, which show better bone ingrowth and mechanical interlocking [6,7]. Another convenient approach is to produce Ti alloys with low Young's modulus by rational alloy design [8]. Recently, metastable β Ti alloys have attracted considerable interest because of low Young's modulus [9]. To maintain good biocompatibility, nontoxic β -stabilizing elements are good option in designing new metastable β -type Ti with good inherent performance.

Molybdenum (Mo), a strong β -phase stabilizing element, is generally considered nontoxic and nonallergic at low concentrations [10]. With a high melting temperature, Mo increases the melting point of Ti–Mo alloys, and consequently the difficulty of material processing. In Ti–Mo alloys, 10% Mo

is the minimum amount to retain the β -phase [11]. Mo reduces the Young's modulus of alloys while increases the strength, wear resistance, and corrosion resistance [11–14]. In binary Ti–Mo alloys with 6–20% Mo, the solid solution hardening effect of Mo is maximal when the content is 10–12% [11]. Taking these aspects into consideration, 12% Mo is chosen in this study. Actually, several studies have investigated the corrosion resistance of Ti–12Mo in different environments [15,16]; however, whether it is appropriate for bone repair is far from fully understood due to the lack of *in vivo* studies.

Also recognized as a nontoxic and nonallergic element for human being, zirconium (Zr) and Ti are in the same group of the element periodic table. The crystal structure of Zr is similar to that of Ti. Previous studies demonstrated that pure Zr showed more bone-implant contact than that of Ti *in vivo* [17]. With a great solubility in the crystalline of Ti [18], Zr is effective in increasing the mechanical strength of Ti alloys, while it decreases the melting temperature and thus facilitates the casting process [19]. Particularly, binary Ti–Zr alloys have showed encouraging results as dental implants [20,21]. Therefore, it is reasonable to employ Zr as alloying element to improve the performance of commercially pure Ti (CP–Ti).

Until now, several studies have explored the mechanical property and cytocompatibility of binary Ti–Zr or Ti–Mo alloys [22,23], but their potential for bone repair remains unclear, mainly due to the lack of *in vivo* evaluations. Previous studies have investigated the deformation mechanism of several Ti–Mo–Zr alloys [24–30]. Based on their outstanding properties such as high ductility and strength [24,27], we speculate that they may serve as good candidate for orthopedic implants. To address this, systematic *in vitro* and *in vivo* evaluations are conducted in this study to answer the following questions: (1) Does Zr or Mo addition influence the properties relevant to bone repair? (2) Do they have superior properties for bone repair when compared with CP–Ti, a commonly utilized bone implant in the clinic?

2. Materials and methods**2.1. Material preparation**

The alloy ingots including Ti–12Mo, Ti–10Zr, and Ti–12Mo–10Zr (wt %) were melted in a vacuum arc-melting furnace respectively. Pure titanium, molybdenum, and zirconium granules (all with a purity at least 99.5%) were used as raw materials. The cast ingots weighting at about 1 kg per sample were remelted for five times to achieve high homogeneity in chemical composition. Before water quenching, the samples were solution-treated at 1173 K for 30 min in a vertical quenching tubular furnace (quartz tube) under a high vacuum of 2.5×10^{-3} Pa. Before the following experiments, the specimen was ground with water-proof papers (SiC abrasive papers, up to 2500 grit) and then ultrasonic cleaned with ethanol and distilled water respectively.

2.2. Microstructure and composition analysis

To detect the phase constitution of alloys, X-ray diffraction (XRD) analysis was carried out on a Bruker D8 ADVANCE X-

Ray Diffractometer (Germany) with Cu $K\alpha$ radiation ($\lambda = 0.1506$ nm) and 2θ scanning range of $20\text{--}90^\circ$ operating at 40 kV and 30 mA. Optical microscopy (OM, GX53, Olympus) was employed for metallographic observation. The phases were further identified by a scanning electron microscope (SEM, SU3500, Hitachi, Japan), which was equipped with an energy dispersive spectroscopy (EDS) to analyze the chemical composition. After mechanical polishing, samples for OM and SEM observations were polished with a diamond polishing paste (particle size: $0.5\ \mu\text{m}$) and etched with an acidic solution containing H_2O , HNO_3 and HF (5:3:1, vol. %) to reveal the grain boundaries.

2.3. Mechanical properties and microhardness measurement

Specimen for tensile mechanical analyses (dumbbell-like shape, length: 60 mm; width: 10 mm; thickness: 1.5 mm) were prepared from alloy ingots using a wire electrical discharge machine. The mechanical properties of alloys were analyzed on a universal testing machine (Instron 5982, Canton, MA) with a strain rate of $1 \times 10^{-3}\ \text{s}^{-1}$ at room temperature. During the mechanical testing, an extensometer was employed to calibrate the strain. In each sample, the tensile experiment was repeated for three times to ensure the validity. The Young's moduli of samples and their elongation rate were calculated from the strain-stress curves. The microhardness of alloys was measured on a microhardness tester (Wilson VH1102, USA) with a load of 100 g and a dwell time of 10 s. In this test, the samples were first polished by a diamond paste to produce a mirror-like surface for measurement; then, at least 15 indentations were measured in each example.

2.4. Electrochemical corrosion test

An electrochemical workstation (Interface 1010, Gamry, USA), together with a conventional three electrode system, was employed to conduct the electrochemical corrosion experiment. The specimen, platinum electrode, and saturated calomel electrode (SCE) corresponded to the working, counter and reference electrode respectively. Corrosion measurements were conducted at room temperature in phosphate buffer solution (PBS, $\text{pH} = 3.8\text{--}4$). All specimen were processed to a uniform size of $10\ \text{mm} \times 10\ \text{mm} \times 2\ \text{mm}$; in each sample, 1-cm^2 area was exposed, and the remaining surface was covered with epoxy to avoid possible crevice attacks.

Before the electrochemical test, samples were mirror-polished and immersed in PBS for 0.5 h to form a stable passivation film on the surface. Open circuit potential (OCP) was measured for 1 h until stable. When the OCP was stable, following experiments were performed. Firstly, electrochemical impedance spectroscopy (EIS) was conducted at the range of 10^{-2} to 10^5 Hz, along with an AC amplitude of 10 mV. The EIS curves were analyzed with a ZSimpWin software V3.60. Potentiodynamic polarization test was conducted from $-1\ \text{V}$ to $3.5\ \text{V}$ (vs. SCE) with a scan rate of $1\ \text{mV}\ \text{s}^{-1}$. Tafel extrapolation method was applied for data analysis, and the cathodic branch was mainly considered. All electrochemical tests were repeated for three times to ensure data consistency.

2.5. Analysis of passivation film

After immersion of alloys in PBS ($\text{pH} = 4$) for 0.5 h, the chemical composition of passivation film was investigated by an X-ray photoelectron spectroscopy (XPS, ESCALAB 250xi, Thermo Fisher, USA) with Al $K\alpha$ radiation (1486.6 eV). The instrument was operated at constant energy mode, with a pass energy of 20 eV and an X-ray spot size of $900\ \mu\text{m}$. The XPS spectra of elements were analyzed with an XPSPEAK V41 software. Binding energy was calibrated with C 1s at 284.8 eV.

2.6. Cytocompatibility assessment

The cytocompatibility of alloys was examined by culturing MC3T3-E1 cells on their surface. CP-Ti served as the control. The specimens were cut into square plates ($10\ \text{mm} \times 10\ \text{mm}$), and their surface was polished with SiC papers (grit 240 to 2500). After sequential cleaning with acetone, ethanol, and deionized water under sonication (15 min per treatment), the samples were sterilized in an autoclave. MC3T3-E1 cells were cultured in Dulbecco's modified Eagle's medium supplemented with 10% fetal bovine serum and 1% penicillin/streptomycin at $37\ ^\circ\text{C}$, 5% CO_2 , and 95% humidity. The medium was replaced every 48 h, and cells were passaged at 80% confluency.

MC3T3-E1 cells were seeded on the surface of alloys at the density of 2×10^4 cells/mL. After culture for 1, 3 and 5 days, the cells were washed twice with PBS, and stained with the working solution of Live/Dead staining kit (BestBio, Shanghai, China) for 5 min at $37\ ^\circ\text{C}$ in the dark. Then the cells were rinsed with PBS for three times and observed under a fluorescence microscope with the excitation wavelength of 518 nm. The number of live and dead cells were counted in three random fields per sample at the magnification of $\times 200$ using an Image J software (V1.8.0, National Institutes of Health, Bethesda, MD, USA). The proliferation of cells was measured by Cell Counting Kit-8 (CCK-8, Dojindo, Japan). At each time point, $10\ \mu\text{l}$ of CCK-8 test solution was added, and the cells were incubated for 1.5 h in the dark. The absorbance at 450 nm was measured using an enzyme-linked immunosorbent assay microplate reader. The experiment was repeated three times.

2.7. Animal experiments

All animal experiments were performed according to the international guidance on animal welfare and were approved by the Animal Research Committee of the State Key Laboratory of Oral Diseases, West China School of Stomatology, Sichuan University. Twenty-one Sprague Dawley rats (female, 3-month-old, weighing at 210–230 g) were randomly divided into the following groups: 1) CP-Ti group, 2) Ti–12Mo group, and 3) Ti–12Mo–10Zr group. The alloys were cut into cylindrical rods with a diameter of 1 mm and a length of 10 mm. The specimens were polished with SiC papers before cleaning and sterilization.

After general anesthesia through abdominal injection of pentobarbital (3%, 30 mg/kg, Sigma, USA), each rat received two implants at the proximal tibia. To form a channel, a 1.0 mm hole was drilled perpendicularly from the articular surface of tibia. The implants were inserted into the channels below the articular surface. After implantation for eight

Table 1 – Elemental composition of Ti–Mo–Zr alloys.

Alloy	Ti (wt %)	Mo (wt %)	Zr (wt %)
Ti–10Zr	90.31	/	9.69
Ti–12Mo	88.60	11.40	/
Ti–12Mo–10Zr	78.7	11.53	9.77

weeks, tibiae with implants were harvested for further analysis.

2.7.1. Micro-CT analysis

New bone formation was observed using a high-resolution μ -CT scanning system (Scanco Medical μ -CT 50, Switzerland). The volume of interest (VOI) was defined as the entire area around implants, extending from 2 mm below the epiphyseal plate to the distal 100 layers. After scanning, 3D model was reconstructed with a visualization software CTVol (SkyScan). After VOI reconstruction, the following parameters were calculated, including bone volume/total sample volume (BV/TV), mean trabecular thickness (Tb. Th), and bone-implant-contact (BIC), which was defined as the ratio of bone in direct contact with the implant to the total lateral surface area of implant.

2.7.2. Biomechanical test

After Micro-CT analysis, biomechanical test was performed on a universal material testing system (Instron 4302, USA). Compression force was applied at the distal end of implants, with a speed of 1 mm/min. The curve of displacement and force was recorded, and the maximum push-out force was calculated.

2.7.3. Histological observation

After fixed in 4% neutral formalin buffer for 48 h, the samples were taken for histological observation without decalcification. They were dehydrated in gradient ethanol (40–100%) and embedded in methyl methacrylate. Sections with a thickness of 100 μ m were prepared perpendicular to the long axis of implants, grounded into 70 μ m thick, and stained with 1% toluidine blue. The sections about 1 mm below the growth plate were observed, and the bone area ratio (i.e., the percentage of mature bone within a ring region extending 250 μ m from the implant surface) was analyzed.

2.8. Statistical analysis

All data were expressed as the mean \pm standard deviation. Data were analyzed by SPSS software (version 21.0, IBM Corp, Armonk, NY). One-way ANOVA and Student-Newman-Keuls multiple comparison test were applied to compare the difference between groups. $P < 0.05$ was considered statistically significant.

3. Results and discussion

3.1. Phase composition and microstructure

Table 1 shows the chemical composition of prepared alloys. The elements are in concentrations close to the stoichiometry of alloys, with negligible quantity of impurity.

Fig. 1 shows the XRD pattern of alloys, which are similar to previous studies [11,31–33]. Ti–10Zr presented only peaks of a martensitic α' phase with a distorted hexagonal structure. Ti–12Mo and Ti–12Mo–10Zr revealed only peaks of equiaxial β phase. It is noteworthy that, compared with the peaks of α - or β -phase of Ti, those peaks associated with the α' phase of Ti–10Zr, as well as those associated with the β phase of Ti–12Mo–10Zr, shifted towards a lower angle respectively. This can be ascribed to an increase in the lattice constant of alloys, which is possibly induced by the larger atomic radius of Zr element (0.160 nm) than that of Ti element (0.147 nm) [31].

The microstructure of alloys was observed by OM and SEM respectively. As shown in Fig. 2, a fine acicular-shaped structure was noted in Ti–10Zr, which is the characteristic structure of α' phase. In Ti–12Mo and Ti–12Mo–10Zr, only a coarse β phase was observed. Ti–12Mo presented irregular rough β phase grains with the size of about 500 μ m, while Ti–12Mo–10Zr showed equiaxed β phase grains with the size of 300–500 μ m. Large size of grains can be ascribed to the great driving force for grain growth at high temperature [34]. These micrographs corroborate well with the XRD results, indicating the β -stabilizing action of Mo and Zr elements.

It is known that Mo is a strongly β -stabilizing element that can stable the β phase of Ti when exceeding 10 wt%, which classifies the alloy in the category of β -type Ti [32]. Zr is usually considered as a neutral element; however, when a β -stabilizing element (such as Mo) coexists in the alloys, Zr play a β -stabilizing role [32,35]. In addition, it has been shown that the addition of 6 wt% Zr produces an equivalent β -stabilizing effect to that of 1.5 wt% Mo [36]. The results in this study indicated the presence of β phase in Ti–12Mo–10Zr, which proved the β -stabilizer action of Zr element in solid solution.

3.2. Mechanical properties

3.2.1. Microhardness

The microhardness of Ti–Mo–Zr alloys is displayed in Fig. 3. All alloys exhibited a higher microhardness than that of CP-Ti

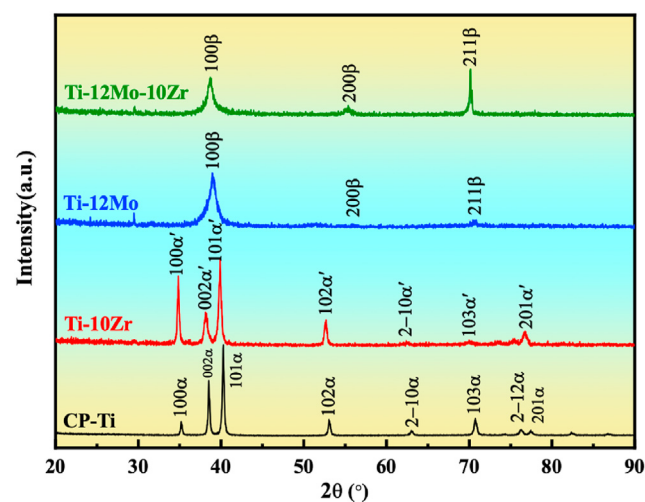


Fig. 1 – XRD pattern of Ti–Mo–Zr alloys. CP-Ti served as the control.

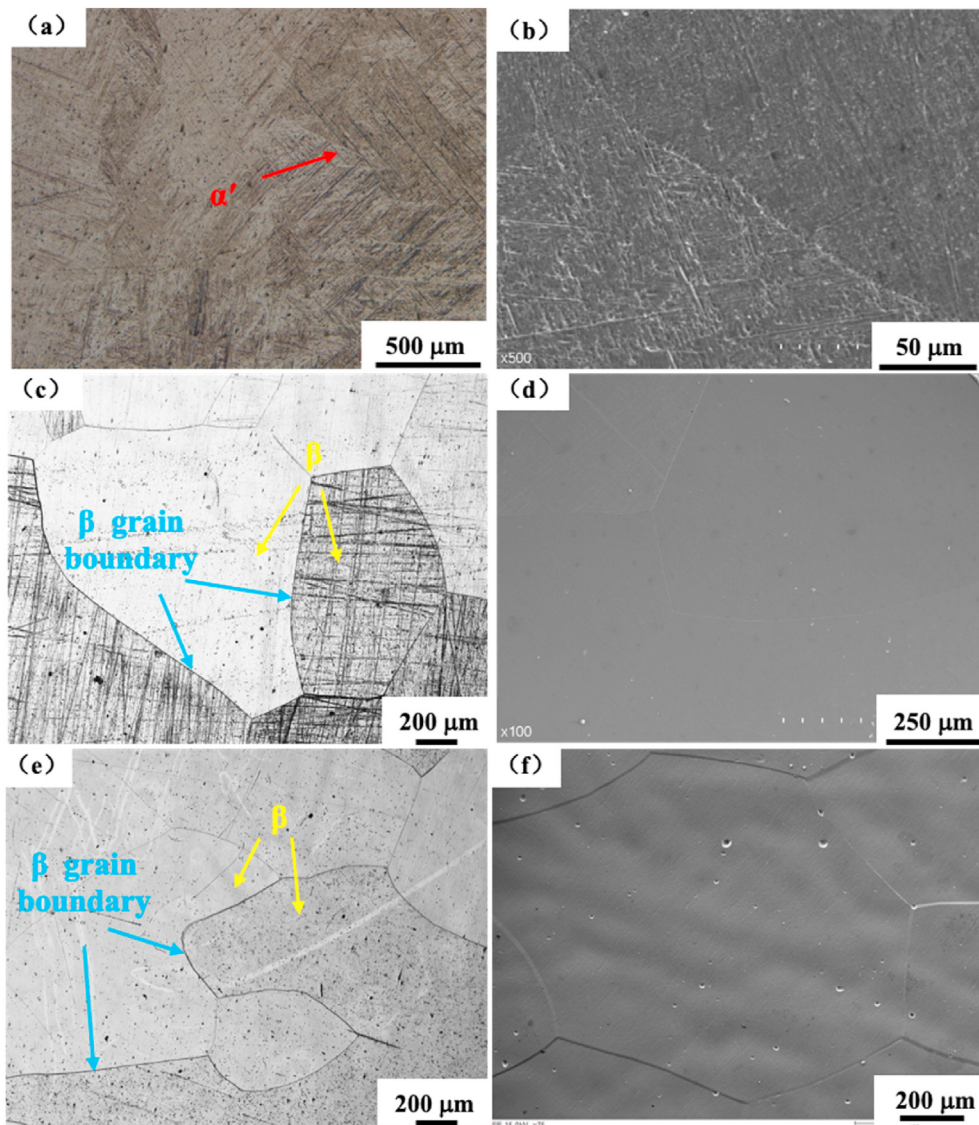


Fig. 2 – Optical and SEM images of Ti–Mo–Zr alloys. (a, b) Ti–10Zr; (c, d) Ti–12Mo; (e, f) Ti–12Mo–10Zr. Left column: optical images; right column: SEM images.

(213 ± 8 HV), because of the crystalline lattice distortion and the solid solution hardening effect of Zr and Mo elements [11,22,32,33,35]. Due to the intrinsic microstructural contributions, Ti–10Zr presented the lowest microhardness among the Ti–Mo–Zr alloys which can be ascribed to the phenomenon that β phase generally has a higher microhardness than that of α' phase, probably due to a stronger solid solution effect [11]. Similarly, in the binary Ti–Mo alloys, Ho et al. reported that β phase alloys possessed a higher microhardness than those alloys with other phases [11]. However, it is worth noting that the microhardness of Ti–10Zr is still much higher than that of CP-Ti (about 1.34 times). Similar results have been reported in Ti–15Zr–xMo alloys [37]. The microhardness of Ti–12Mo–10Zr (318 ± 10 HV) was slightly higher than that of Ti–12Mo (301 ± 7 HV), which is ascribed to the increased solid solution effect of joint Zr and Mo elements [37]. It has also been reported that the grain size of alloys can affect their mechanical properties [38]. Compared to Ti–12Mo (with a

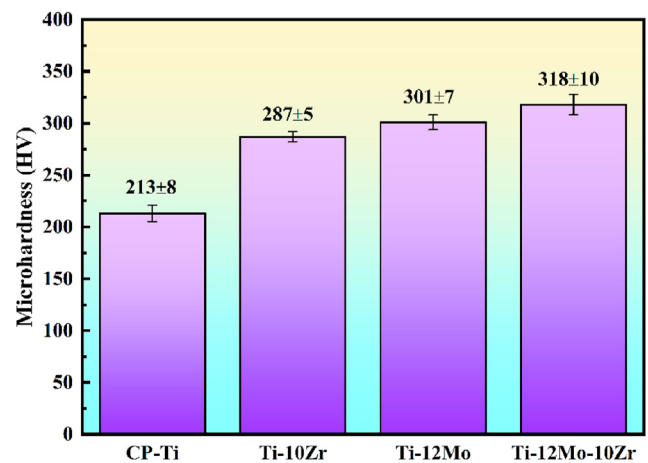


Fig. 3 – Microhardness of Ti–Mo–Zr alloys. CP-Ti served as the control.

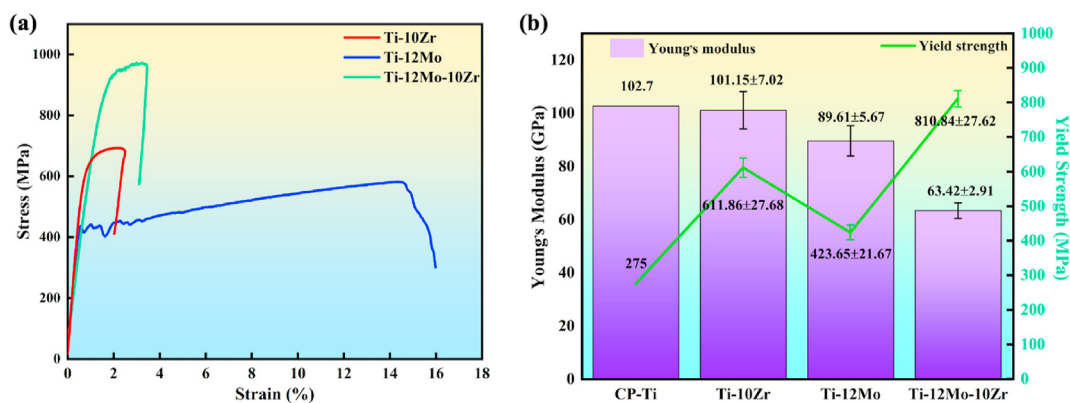


Fig. 4 – The Young's modulus and yield strength of Ti–Mo–Zr alloys. (a) Tensile stress-strain curves; (b) Young's modulus and yield strength. CP-Ti served as the control. Data of CP-Ti are cited from Ref. [40].

grain size of $\sim 500 \mu\text{m}$), Ti–12Mo–10Zr showed a smaller grain size ($300\text{--}500 \mu\text{m}$), which can induce fine grain strengthening and lead to higher microhardness [39].

3.2.2. Mechanical properties

The Young's modulus of bone implants should be closer to that of bone ($10\text{--}30 \text{ GPa}$). The tensile stress-strain curve, the Young's modulus, and the yield strength of Ti–Mo–Zr alloys are presented in Fig. 4. It is shown that the prepared Ti–Mo–Zr alloys possess lower Young's modulus ($63\text{--}101 \text{ GPa}$) and higher yield strength ($423\text{--}810 \text{ MPa}$) than those of CP-Ti (Young's modulus: 102.7 GPa , yield strength: 275 MPa , Fig. 4b) [40]. As an intrinsic property of materials, Young's modulus of alloys is determined by the bonding force between atoms [22]. The bonding force is related to the crystal structure and the distance between atoms, and it will be affected by the addition of alloying elements and heat treatment [22]. Because the atomic radius of Zr is greater than that of Ti, the Young's modulus of Ti–10Zr is lower than that of CP-Ti [22,41]. Previous studies reported that the body-centered cubic structure in β phase alloys exhibits a lower bonding force among atoms, which ensures a reduced Young's modulus [22,32,41,42]. Therefore, as β phase alloy, Ti–12Mo and Ti–12Mo–10Zr possess a much lower Young's modulus than those of CP-Ti and Ti–10Zr. Compared with Ti–12Mo, Ti–12Mo–10Zr exhibited a lower Young's modulus, which can be originated from the β stabilizing function of Zr element [32,35,36,41,42].

A combination of high strength and low Young's modulus is beneficial for minimizing the stress shielding effect of bone implants [41]. Moreover, high strength avoids the fracture of implants under long-term complex stress *in vivo*. In this study, the yield strength of Ti–Mo–Zr alloys ($423\text{--}810 \text{ MPa}$) was much higher than that of CP-Ti (275 MPa) (Fig. 4b) [40], which is very attractive for bone implants. Furthermore, the ultimate tensile strength of Ti–10Zr, Ti–12Mo and Ti–12Mo–10Zr were $693.00 \pm 10.5 \text{ MPa}$, $580.62 \pm 23.82 \text{ MPa}$, and $972.38 \pm 45 \text{ MPa}$ respectively, which were also much higher than that of CP-Ti ($345 \pm 34 \text{ MPa}$). Based on these, the Ti–Mo–Zr alloys are expected to possess strong ability to avoid fracture *in vivo*.

Besides, a suitable elasticity of alloys is desirable for producing bone implants with complex geometry. In this study, the fracture elongation rates of prepared Ti–Mo–Zr alloys

were determined. The results showed that Ti–10Zr, Ti–12Mo and Ti–12Mo–10Zr possess a fracture elongation rate of $2.18 \pm 0.36\%$, $14.51 \pm 0.37\%$ and $3.24 \pm 0.35\%$ respectively. This outcome revealed that the addition of Zr element decreased the elastoplasticity of Ti–12Mo, while the addition of Mo element increased the elastoplasticity of Ti–10Zr.

Taken together, among the prepared Ti–Mo–Zr alloys, Ti–12Mo–10Zr showed the best comprehensive mechanical properties for bone repair due to the low Young's modulus and high yield strength.

3.3. Electrochemical characterization

3.3.1. Potentiodynamic polarization

The potentiodynamic polarization curves of Ti–Mo–Zr alloys are demonstrated in Fig. 5. A similar polarization pattern is recorded in these alloys, showing that the active solution zone entered directly into the stable passivation zone without any transition zone. This reveals that the studied alloys possess great passivation ability. A uniform passivation region is observed in all alloys, suggesting that a stable passivation film is formed on the surface. Compared with other alloys, a wider

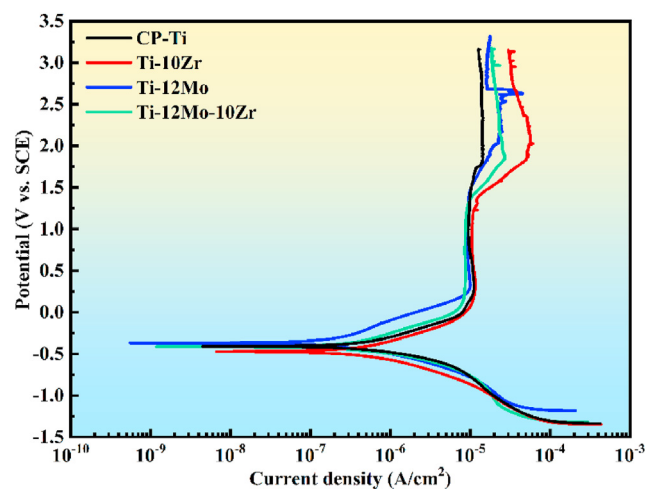


Fig. 5 – Potentiodynamic polarization curves of Ti–Mo–Zr alloys. CP-Ti served as the control.

Table 2 – The corrosion parameters of Ti–Mo–Zr alloys.

Alloy	E_{corr} (mV)	I_{corr} ($\text{nA}\cdot\text{cm}^{-2}$)	I_{pass} ($\mu\text{A}\cdot\text{cm}^{-2}$)	Corrosion rate ($\times 10^{-6}$ mmpy)
CP-Ti	-414	396.5 ± 5.5	9.78 ± 0.24	236.65 ± 8.35
Ti-10Zr	-473	478 ± 11	10.63 ± 0.22	274.9 ± 3.3
Ti-12Mo	-410	362 ± 7.3	9.34 ± 0.17	210.5 ± 4.1
Ti-12Mo-10Zr	-384	353 ± 6	8.68 ± 0.18	204.65 ± 1.85

passivation region is present in Ti-12Mo and Ti-12Mo-10Zr groups, indicating that their passivation ability is more stable than others. At anodic potential higher than 2 V, obvious increases in the current density were observed, which indicate the occurrence of pit corrosion. The corrosion kinetic behavior of prepared Ti–Mo–Zr alloys is similar to other reports [43–45].

The electrochemical corrosion parameters of Ti–Mo–Zr alloys were calculated from the potentiodynamic polarization curves using Tafel extrapolation method (Table 2). The corrosion potential values (E_{corr}) of Ti-10Zr, CP-Ti, Ti-12Mo, and Ti-12Mo-10Zr were -473 mV, -414 mV, -410 mV, and -384 mV respectively. Therefore, the corrosion tendency is in the order of Ti-10Zr > CP-Ti > Ti-12Mo > Ti-12Mo-10Zr. By contrast, their corrosion current density (I_{corr}) and passive current density (I_{pass}) decreased gradually (Table 2). Taken together, the corrosion resistance is in the order of Ti-12Mo-10Zr > Ti-12Mo > CP-Ti > Ti-10Zr.

3.3.2. Electrochemical impedance spectroscopy

The electrochemical impedance spectroscopy (EIS) of Ti–Mo–Zr alloys, coupled with the equivalent circuit model used to fit the EIS results, are displayed in Fig. 6. All alloys showed two capacitive loops in the Nyquist plots (Fig. 6a), which correspond to different capacitive time constant respectively. High-frequency capacitive loops reveal the transferring of charges during the dissolution of metal anodes. Low-frequency capacitive loops reveal the corrosion product film on the surface, and the arcs indicate the inhibition of ion diffusion by corrosion product film. Since larger arc radius means better corrosion resistance, the electrochemical impedance of Ti-12Mo-10Zr, Ti-12Mo, CP-Ti, and Ti-10Zr decreased gradually (Fig. 6a).

Bode plots (Fig. 6b) demonstrate the corrosion feature of alloys at testing frequency. At the range of 10^3 – 10^5 [5] Hz, all alloys showed constant phase and impedance at about 0° and $10^2 \Omega \text{ cm}^2$ respectively, reflecting that the resistance of

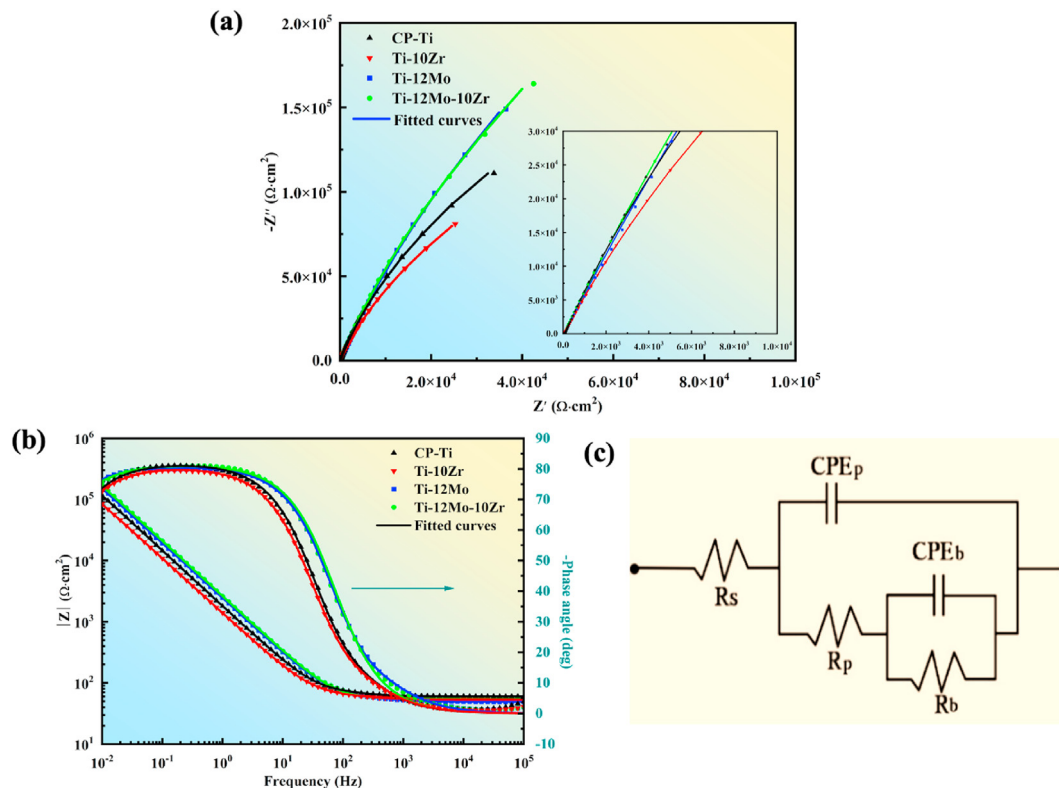


Fig. 6 – EIS of Ti–Mo–Zr alloys. (a) Nyquist plots; (b) Bode plots, which show the result of impedance magnitude to frequency, and the phase angle to frequency; (c) The equivalent circuit model used to fit the impedance spectra of alloys. R_s : resistance of PBS between reference and working electrode; CPE_p : constant phase element (CPE) associated with the outer porous layer of passivate film; R_p : charge transfer resistance associated with the outer porous layer of passivate film; CPE_b : CPE related to the inner compact barrier layer (i.e., the oxide/corrosion product film) of passivate film; R_b : resistance related to the inner compact barrier layer of passivate film. CP-Ti served as the control.

Table 3 – Fitted electrochemical impedance parameters of Ti–Mo–Zr alloys.

Alloy	R_s ($\Omega \cdot \text{cm}^2$)	CPE_p ($\times 10^{-5} \text{S} \cdot \text{sec}^n \cdot \text{cm}^2$)	n_p	R_p ($\Omega \cdot \text{cm}^2$)	CPE_b ($\times 10^{-5} \text{S} \cdot \text{sec}^n \cdot \text{cm}^2$)	n_b	R_b ($\times 10^5 \Omega \text{cm}^2$)	Chi-Squared/ χ [2] ($\times 10^{-4}$)
CP-Ti	60.46	6.242	0.916	48.77	4.173	0.902	8.006	3.73
Ti–10Zr	53.11	7.872	0.898	35.93	6.026	0.895	6.006	1.07
Ti–12Mo	49.01	5.065	0.886	37.13	2.779	0.921	20.45	1.11
Ti–12Mo–10Zr	52.49	3.9655	0.916	32.1	2.186	0.904	25.86	5.61

CPE_b : CPE of inner compact barrier layer; CPE_p : CPE of outer porous layer; n_b : CPE exponent of inner compact barrier layer; n_p : CPE exponent of outer porous layer; R_b : resistance of inner compact barrier layer; R_p : charge transfer resistance of outer porous layer; R_s : resistance of PBS between reference and working electrode.

electrolyte solution was negligible. At the range of 10^{-2} – 10 [2] Hz, a linear relation was observed in the impedance spectrum (Fig. 6b), meaning that the alloys possess excellent corrosion resistance. At 10^{-2} Hz, the impedance modulus of Ti–12Mo–10Zr, Ti–12Mo, CP-Ti and Ti–10Zr decreased gradually, meaning that the corrosion resistance decreased as well. At the range of 10^{-2} – 10 Hz, a wide plateau was observed due to the bi-layered structure of passivation film (Fig. 6b). Furthermore, Ti–12Mo–10Zr showed the highest phase angle, indicating that it possesses the best corrosion resistance. Overall, these EIS results are consistent with potentiodynamic polarization outcomes, showing that the corrosion resistance of Ti–12Mo–10Zr, Ti–12Mo, CP-Ti and Ti–10Zr decreased gradually.

To analyze the electrochemical parameters, an equivalent circuit model (Fig. 6c) was employed to fit the EIS results using a ZsimpWin software. As listed in Table 3, the Chi-squared (χ^2) values were in the order of 10^{-4} , indicating that the fitted results were reliable. Much higher values were recorded in the resistance of inner layer of passivate film (R_b) than that of the outer porous layer (R_p), confirming that the corrosion resistances are closely related to the inner dense layers. In addition, the R_b value of Ti–10Zr, CP-Ti, Ti–12Mo and Ti–12Mo–10Zr increased gradually, meaning that the corrosion resistance of the inner layer of passivate films also increased. Compared with Ti–12Mo and Ti–12Mo–10Zr, higher CPE_p values were noted in Ti–10Zr and CP-Ti, indicating that their outer layer was thinner and the corrosion resistances were weaker. Taken together, fitted results demonstrated that the corrosion resistance is in the order of Ti–12Mo–10Zr > Ti–12Mo > CP-Ti > Ti–10Zr.

3.3.3. XPS characterization

XPS analysis was performed to determine the composition of passive films. Standard binding energy of C 1s peak (284.8 eV) was utilized to calibrate the peaks. Characteristic peaks of Ti 2p, Mo 3 d, Zr 3 d, O 1s, and C 1s were observed (Fig. 7). The high-resolution scan spectrum of these peaks is illustrated respectively.

In the passive film of Ti–10Zr, Ti $2p_{1/2}$ and Ti $2p_{3/2}$ peaks were recorded at 464.31 eV and 458.6 eV respectively (Fig. 8), corresponding to Ti^{4+} oxide. Zr $3d_{3/2}$ and Zr $3d_{5/2}$ peaks were recorded at 184.72 eV and 182.32 eV respectively, corresponding to Zr^{4+} oxide. Three peaks were observed in the O 1s spectrum, including O^{2-} (530.03 eV), OH^- (531.26 eV) and H_2O

(532.43 eV). The H_2O peak was related to bounded water, the O^{2-} peak was related to TiO_2 and ZrO_2 , and the OH^- peak was related to H_2O . Therefore, the passive film was composed of TiO_2 and ZrO_2 , which is similar to other reports [45].

In the passive film of Ti–12Mo, a doublet exists in the Ti 2p spectrum (Fig. 9), with Ti $2p_{3/2}$ at 458.64 eV and Ti $2p_{1/2}$ at 464.36 eV, which were assigned to the Ti–O bond of TiO_2 [23]. In the Mo 3 d spectrum, two doublets were observed: peaks at 232 eV and 226.8 eV were assigned to the Mo–O bond of MoO_2 , while peaks at 234.88 eV and 229.02 eV were due to the Mo–O bond of MoO_3 [23]. In O 1s spectrum, there are three peaks: 1) the peak at 531.9 eV was indicative of adsorbed H_2O ; 2) the peak at 530.91 eV was related to OH^- ; 3) the peak at 530.1 eV was indicative of O^{2-} . These results showed that the passive film was composed of TiO_2 , MoO_2 and MoO_3 .

In the passive film of Ti–12Mo–10Zr (Fig. 10), Ti $2p_{1/2}$ and Ti $2p_{3/2}$ peak were recorded at 464.11 eV and 458.4 eV respectively, and Zr $3d_{3/2}$ and Zr $3d_{5/2}$ peak were observed at 184.5 eV and 182.1 eV respectively. Ti 2p peaks were due to the Ti–O bond of TiO_2 ; Zr 3 d peaks were ascribed to the Zr–O bond of ZrO_2 . Mo 3 d spectrum contained two doublets: 234.68 eV (Mo $3d_{5/2}$) and 231.81 eV (Mo $3d_{3/2}$) corresponded to MoO_2 , while 235.36 eV (Mo $3d_{5/2}$) and 232.09 eV (Mo $3d_{3/2}$) was assigned to MoO_3 [23]. The O 1s spectra contained three peaks: 531.72 eV

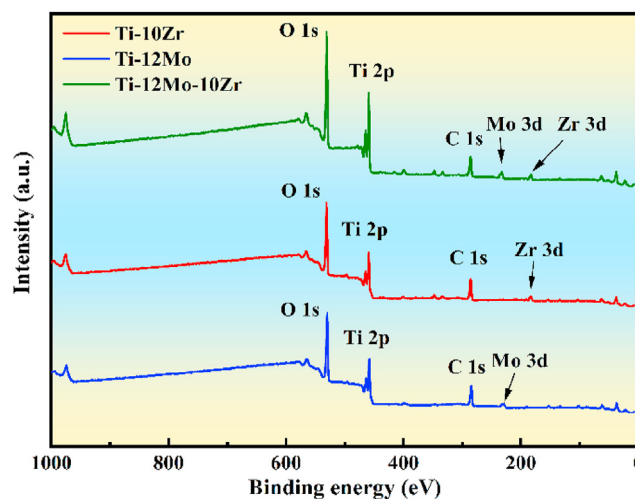


Fig. 7 – XPS spectrum of the passive film of Ti–Mo–Zr alloys.

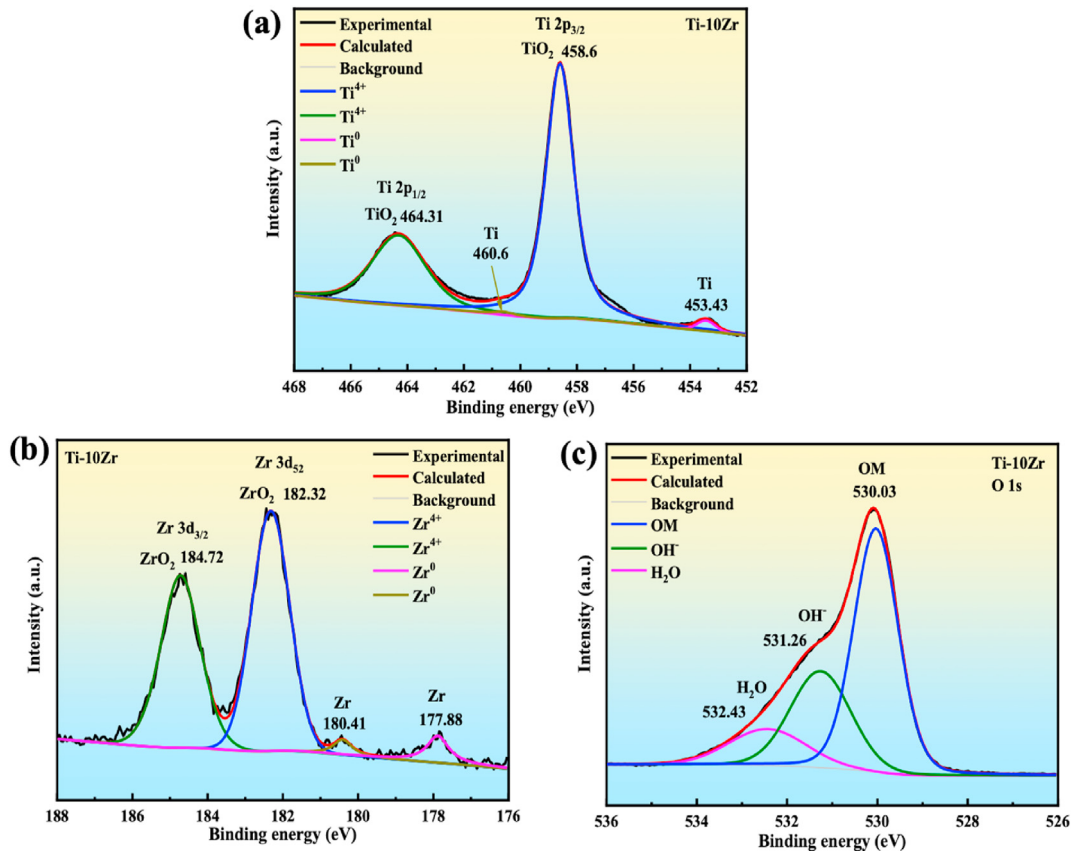


Fig. 8 – High-resolution XPS spectrum of the passive film of Ti–10Zr. (a) Ti 2p; (b) Zr 3 d; (c) O 1s.

was indicative for absorbed H_2O , 530.55 eV was related to OH^- , and 529.87 eV was corresponded to TiO_2 , ZrO_2 , MoO_2 and MoO_3 .

3.4. Cytocompatibility assay

The cytocompatibility of Ti–Mo–Zr alloys was determined by the viability and proliferation of MC3T3-E1 cells grown on the surface. In Live/Dead staining results (Fig. 11a & b), a number of live cells with a spindle-like shape and obvious cell-cell junctions were observed in all alloys. Importantly, dead cells were not observed during the cell culture period. A progressive increase in the cell number was noted in each group (Fig. 11a & b). Particularly, on day 3, the number of cells in CP-Ti was significantly less than those in the Ti–Mo–Zr alloys ($P < 0.05$); however, no significant difference was observed among groups on days 1 and 5 ($P > 0.05$).

Similarly, in the CCK-8 results, the optical density increased steadily in a time-dependent manner (Fig. 11c). On day 3, the OD values of the Ti–Mo–Zr alloys were slightly higher than that of CP-Ti ($P > 0.05$). According to previous reports [16], the cytotoxicity of CP-Ti is at the grade of 0–1; therefore, based on our results, the cytotoxicity of Ti–Mo–Zr alloys is close to grade 0–1. Taken together, the Ti–Mo–Zr alloys prepared in this study are non-cytotoxic, with a cytocompatibility level similar to that of CP-Ti.

3.5. Osteointegration evaluation

The osteointegration of bone implants is defined as a direct structural and functional connection between the implants and surrounding bone [46], which is critical for bone-implant stability and the long-term success of implants. According to above results, Ti–12Mo and Ti–12Mo–10Zr possess superior mechanical and corrosion resistance properties for bone repair; however, the *in vivo* performance remains unknown. To further determine their potential for future applications, the osteointegration of these alloys was determined by micro-CT analysis, histological staining and push-out test.

According to the micro-CT results, abundant bone tissue was observed around the implant in each group (Fig. 12a). The BV/TV and Tb·Th values in Ti–12Mo and Ti–12Mo–10Zr were slightly higher than those of CP-Ti ($p > 0.05$, Fig. 12b). Compared with CP-Ti, Ti–12Mo showed a much higher BIC ratio ($p < 0.05$); likewise, the BIC value in Ti–12Mo–10Zr was also higher than that of Cp-Ti ($p > 0.05$, Fig. 12b). These results revealed that, when compared with CP-Ti, more bone tissue was formed in the metastable β -type alloys.

Besides micro-CT analysis, toluidine blue staining was applied to observe new bone formation on the surface of implants. As shown in Fig. 13a, newly formed bone tissue was in direct contact with the implants in each group; furthermore, Ti–12Mo and Ti–12Mo–10Zr showed a higher bone area ratio

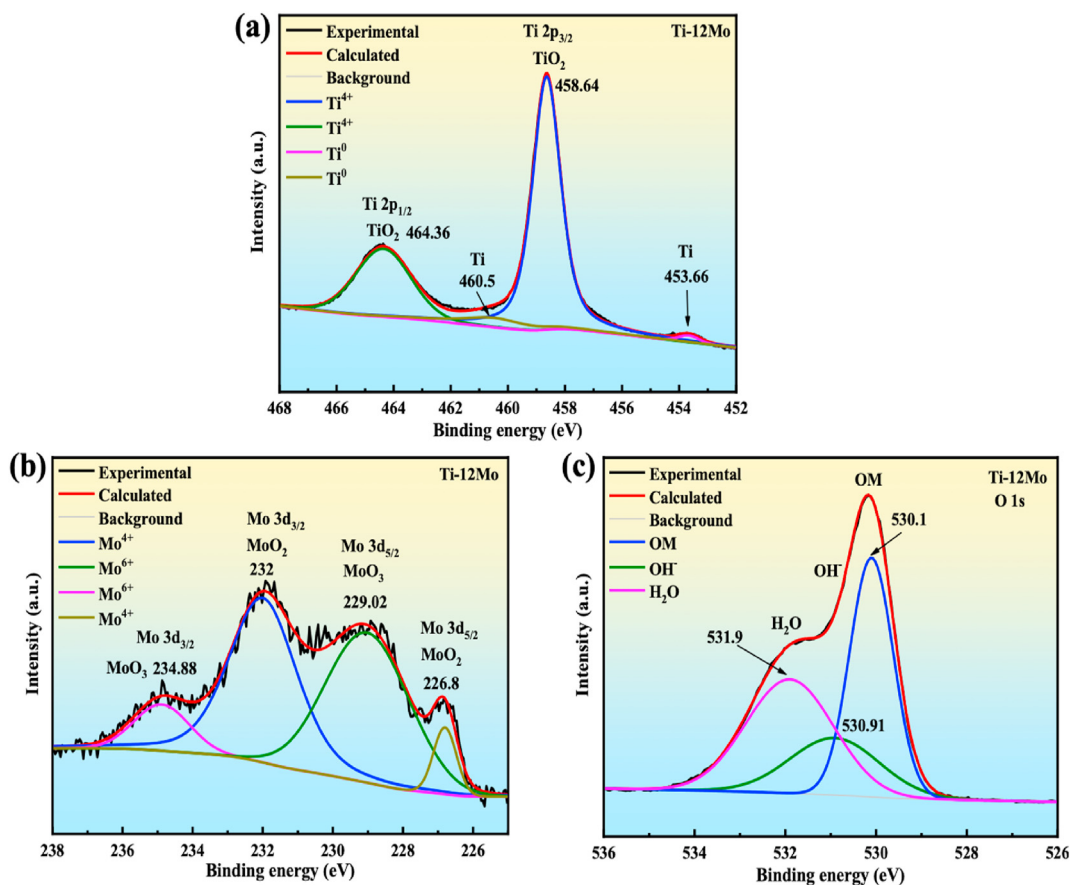


Fig. 9 – High-resolution XPS spectrum of the passive film of Ti–12Mo. (a) Ti 2p; (b) Mo 3 d; (c) O 1s.

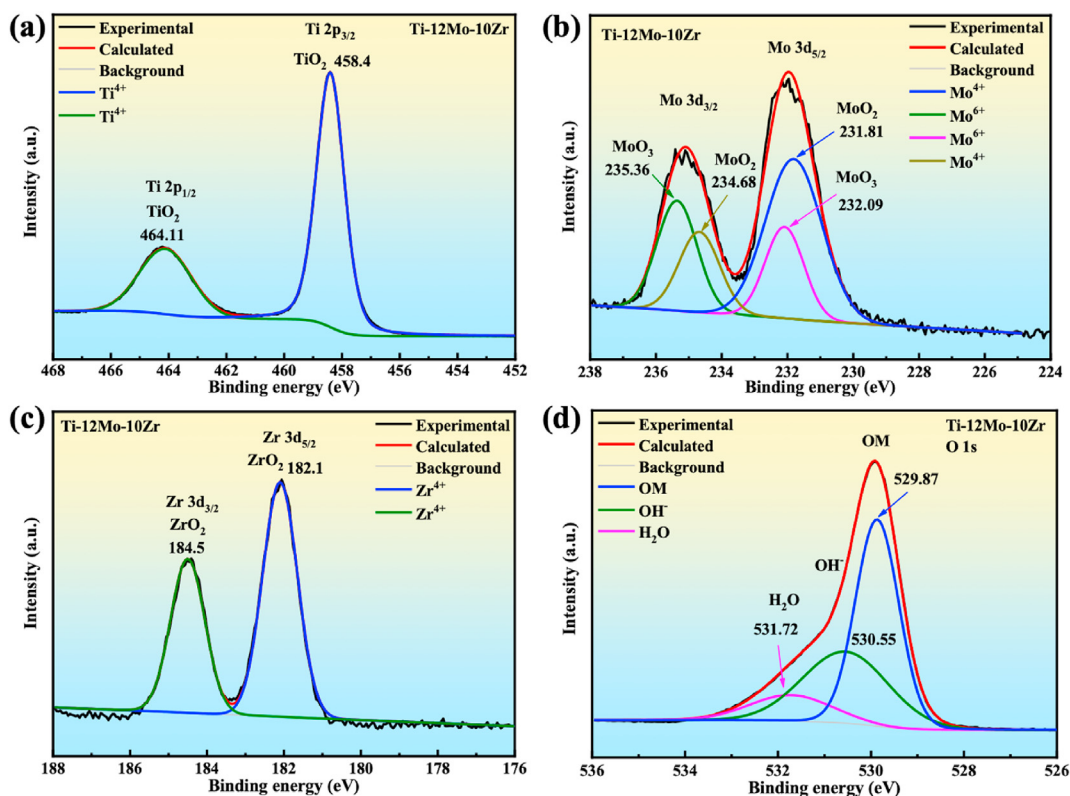


Fig. 10 – High-resolution XPS spectrum of the passive film of Ti–12Mo–10Zr. (a) Ti 2p; (b) Mo 3 d; (c) Zr 3 d; (d) O 1s.

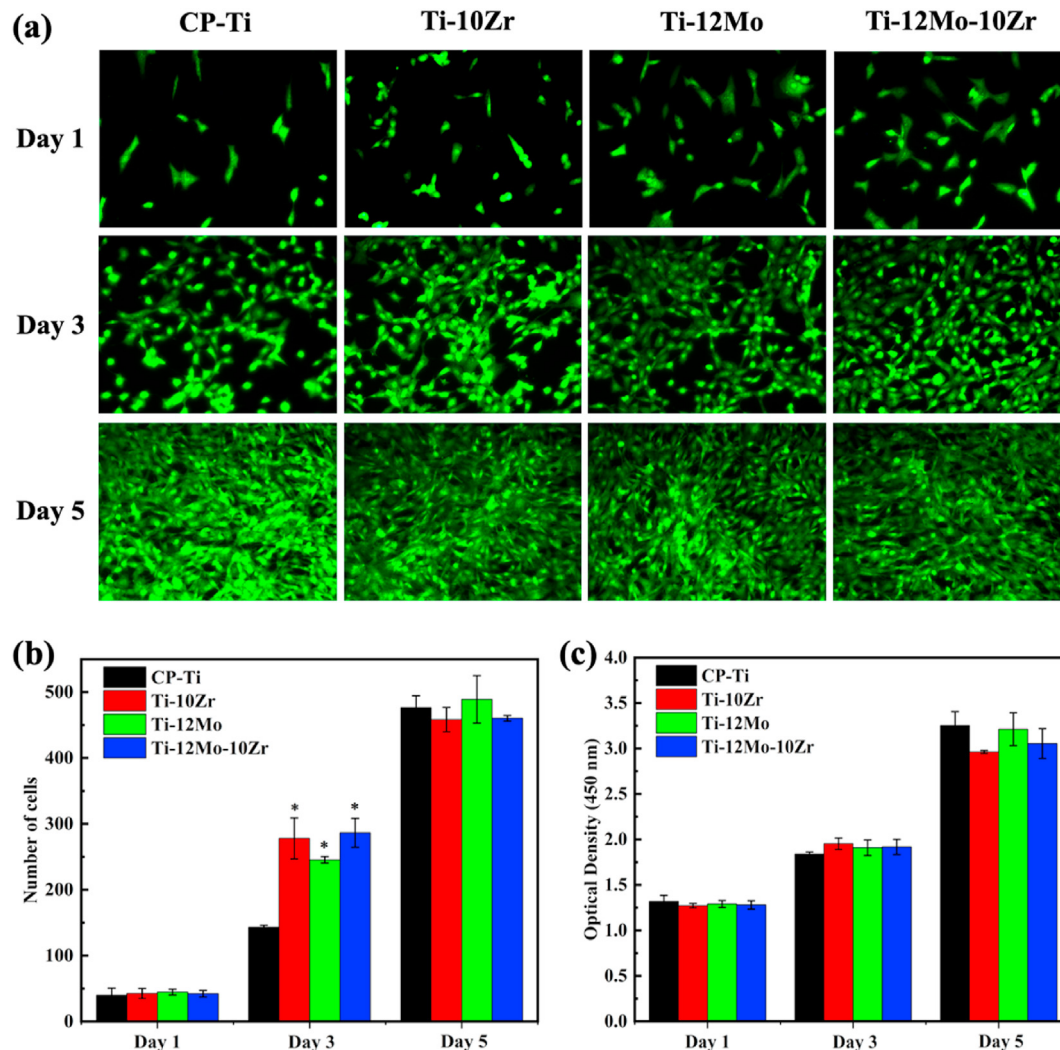


Fig. 11 – Cytocompatibility of Ti–Mo–Zr alloys. (a) Representative images of Live/Dead staining (200 ×). Green fluorescence: living cells; Red fluorescence: dead cells. (b) The number of live cells counted in three random fields per sample in each group. (c) The proliferation of cells measured by CCK-8 assay. CP-Ti served as the control. *: $P < 0.05$ when compared with CP-Ti.

than that of CP-Ti ($p > 0.05$, Fig. 13b). After biomechanical test, it is found that the maximum push-out force was comparable in Ti-12Mo and Ti-12Mo-10Zr, and they are not statistical different from that of CP-Ti ($p > 0.05$, Fig. 13c). Taken together, it is evident that Ti-12Mo and Ti-12Mo-10Zr possess a comparable osteointegration to that of CP-Ti, indicating that they are good alternative to CP-Ti for bone repair.

4. Conclusion

In this study, three Ti–Mo–Zr alloys with different chemical composition were designed and fabricated for biomedical applications. The influence of Mo and Zr addition on the performance of alloys for bone repair was explored for the first

time. Depending on the alloying elements, the studied alloys showed different microstructures. Ti-10Zr shows an acicular-shaped α' phase structure, while Ti-12Mo and Ti-12Mo-10Zr only contain a coarse metastable β phase structure. Among them, Ti-12Mo-10Zr possess the best comprehensive mechanical properties. The Young's modulus was 38% lower than that of CP-Ti, while the microhardness and yield strength were 49% and 194% higher than those of CP-Ti respectively. The corrosion resistance of alloys is in the order of Ti-12Mo-10Zr > Ti-12Mo > CP-Ti > Ti-10Zr. Furthermore, the cytocompatibility and osteointegration of the designed Ti–Mo–Zr alloys are similar to that of CP-Ti. Taken together, this study provides a solid basis for the future clinical translation of Ti–Mo–Zr alloys, especially the Ti-12Mo-10Zr for bone repair.

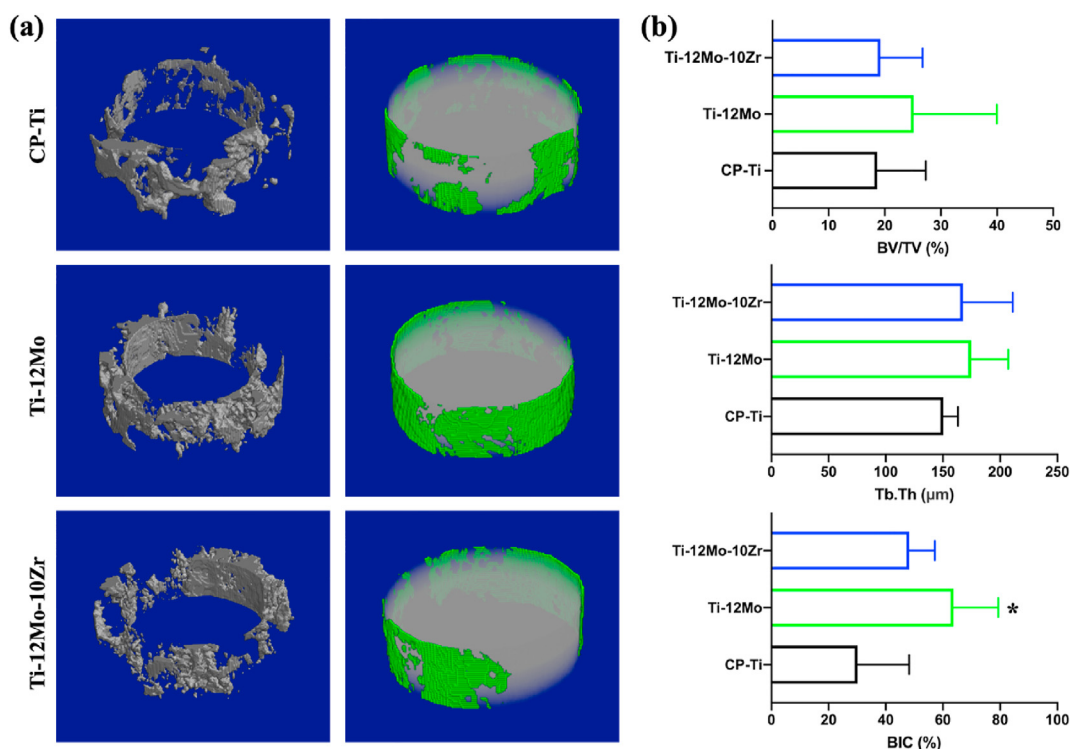


Fig. 12 – Micro-CT analysis of new bone formation after implantation in the tibia of rats. (a) Micro-CT images. Left column: bone volume around implants; right column: bone tissue in direct contact with implants. (b) Quantitative analysis of micro-CT results. BV: bone volume; TV: total volume; Tb.Th: trabecular thickness; BIC: bone-implant-contact. *: $p < 0.05$ when compared with CP-Ti.

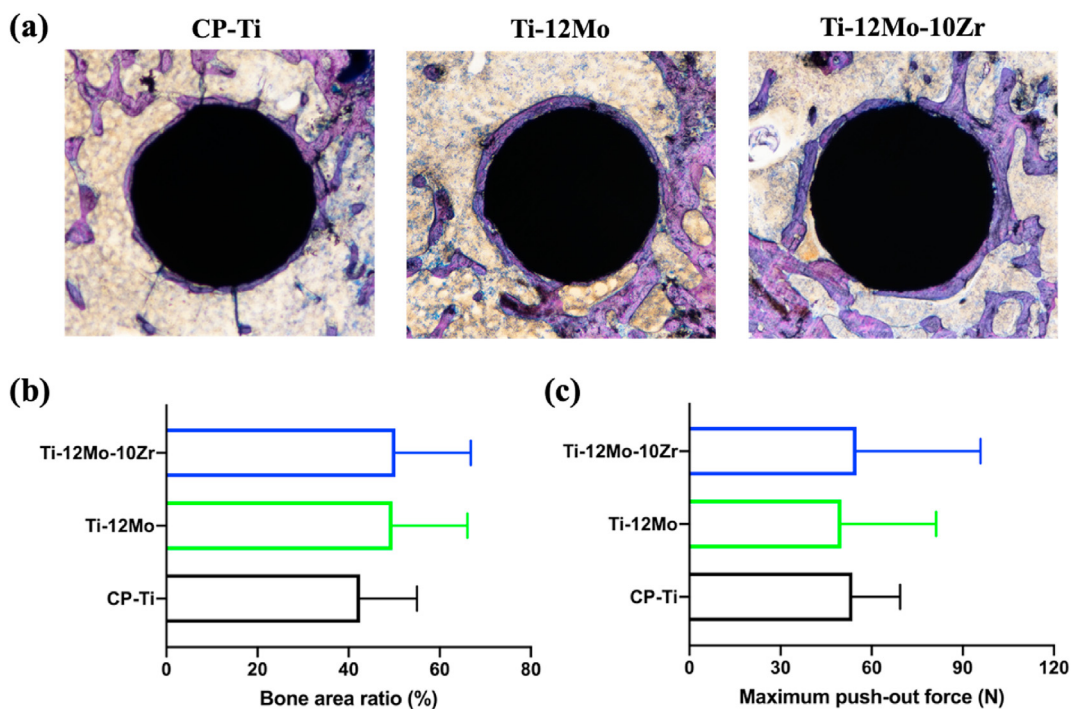


Fig. 13 – Histological staining and biomechanical test of alloys after implantation in rat tibia. (a) Representative image of toluidine blue staining of peri-implant bone tissue. (b) Bone area ratio in each group; (c) The maximum push-out force of implants measured at eight weeks after surgery.

Availability of data and materials

All data generated or analyzed during this study are included in this published article.

Funding

This work was supported by the National Natural Science Foundation of China (52001324), the Natural Science Foundation of Jiangsu Province (BK20200643), the Key Research and Development Program of Henan Province (222102310441), China, and Fundamental Research Funds for the Central Universities (2242023K40029).

Declaration of competing interest

The authors declare that they have no known competing financial interests or personal relationships that could have appeared to influence the work reported in this paper.

Acknowledgements

Not applicable.

REFERENCES

- Boyce RA. Prosthodontic principles in dental implantology: adjustments in a coronavirus disease-19 pandemic-battered economy. *Dent Clin* 2021;65(1):135–65.
- Mantripragada VP, Lecka-Czernik B, Ebraheim NA, Jayasuriya AC. An overview of recent advances in designing orthopedic and craniofacial implants. *J Biomed Mater Res* 2013;101(11):3349–64.
- Li Y, Yang C, Zhao H, Qu S, Li X, Li Y. New developments of Ti-based alloys for biomedical applications. *Materials* 2014;7(3):1709–800.
- Abdel-Hady Gepreel M, Niinomi M. Biocompatibility of Ti-alloys for long-term implantation. *J Mech Behav Biomed Mater* 2013;20:407–15.
- Shah FA, Omar O, Suska F, Snis A, Matic A, Emanuelsson L, et al. Long-term osseointegration of 3D printed CoCr constructs with an interconnected open-pore architecture prepared by electron beam melting. *Acta Biomater* 2016;36:296–309.
- McGilvray KC, Easley J, Seim HB, Regan D, Berven SH, Hsu WK, et al. Bony ingrowth potential of 3D-printed porous titanium alloy: a direct comparison of interbody cage materials in an in vivo ovine lumbar fusion model. *Spine J* 2018;18(7):1250–60.
- Ran Q, Yang W, Hu Y, Shen X, Yu Y, Xiang Y, et al. Osteogenesis of 3D printed porous Ti6Al4V implants with different pore sizes. *J Mech Behav Biomed Mater* 2018;84:1–11.
- Sidhu SS, Singh H, Gepreel MA. A review on alloy design, biological response, and strengthening of beta-titanium alloys as biomaterials. *Mater Sci Eng C Mater Biol Appl* 2021;121:111661.
- Niinomi M, Liu Y, Nakai M, Liu H, Li H. Biomedical titanium alloys with Young's moduli close to that of cortical bone. *Regen Biomater* 2016;3(3):173–85.
- Li Y, Wong C, Xiong J, Hodgson P, Wen C. Cytotoxicity of titanium and titanium alloying elements. *J Dent Res* 2010;89(5):493–7.
- Ho WF, Ju CP, Lin JH. Structure and properties of cast binary Ti-Mo alloys. *Biomaterials* 1999;20(22):2115–22.
- Gonzalez EG, M.-R JC. Study of the corrosion behavior of titanium and some of its alloys for biomedical and dental implant applications. *J Electroanal Chem* 1999:109–15.
- Sochacka P, Miklaszewski A, Jurczyk M. Development of β -type Ti-x at. % Mo alloys by mechanical alloying and powder metallurgy: phase evolution and mechanical properties ($10 \leq x \leq 35$). *J Alloys Compd* 2019;776:370–8.
- Xu W, Yu A, Lu X, Tamaddon M, Ng L, Hayat Md, et al. Synergistic interactions between wear and corrosion of Ti-16Mo orthopedic alloy. *J Mater Res Technol* 2020;9(5):9996–10003.
- Raganya L, Moshokoa N, Obadele BA, Olubambi PA, Machaka R. Investigation of the tensile properties of heat treated Ti-Mo alloys. *Mater Today Proc* 2021;38:1044–8.
- Xu W, Lu X, Wang LN, Shi ZM, Lv SM, Qian M, et al. Mechanical properties, in vitro corrosion resistance and biocompatibility of metal injection molded Ti-12Mo alloy for dental applications. *J Mech Behav Biomed Mater* 2018;88:534–47.
- Guglielmotti MB, Renou S, Cabrini RL. A histomorphometric study of tissue interface by laminar implant test in rats. *Int J Oral Maxillofac Implants* 1999;14(4):565–70.
- Thibon I, Ansel D, Gloriant T. Interdiffusion in β -Ti-Zr binary alloys. *J Alloys Compd* 2009;470(1–2):127–33.
- Ho W-F, Cheng C-H, Chen W-K, Wu S-C, Lin H-C, Hsu H-C. Evaluation of low-fusing porcelain bonded to dental cast Ti-Zr alloys. *J Alloys Compd* 2009;471(1–2):185–9.
- Ou P, Hao C, Liu J, He R, Wang B, Ruan J. Cytocompatibility of Ti-xZr alloys as dental implant materials. *J Mater Sci Mater Med* 2021;32(5):50.
- Grandin HM, Berner S, Dard M. A review of titanium zirconium (TiZr) alloys for use in endosseous dental implants. *Materials* 2012;5(8):1348–60.
- Correa DR, Vicente FB, Donato TA, Arana-Chavez VE, Buzalaf MA, Grandini CR. The effect of the solute on the structure, selected mechanical properties, and biocompatibility of Ti-Zr system alloys for dental applications. *Mater Sci Eng C Mater Biol Appl* 2014;34:354–9.
- Xu JL, Tao SC, Bao LZ, Luo JM, Zheng YF. Effects of Mo contents on the microstructure, properties and cytocompatibility of the microwave sintered porous Ti-Mo alloys. *Mater Sci Eng C Mater Biol Appl* 2019;97:156–65.
- Sun F, Zhang JY, Marteleur M, Brozek C, Rauch EF, Veron M, et al. A new titanium alloy with a combination of high strength, high strain hardening and improved ductility. *Scripta Mater* 2015;94:17–20.
- Sun F, Zhang JY, Vermaut P, Choudhuri D, Alam T, Mantri SA, et al. Strengthening strategy for a ductile metastable β -titanium alloy using low-temperature aging. *Materials Research Letters* 2017;5(8):547–53.
- Zhang JY, Li JS, Chen Z, Meng QK, Sun F, Shen BL. Microstructural evolution of a ductile metastable β titanium alloy with combined TRIP/TWIP effects. *J Alloys Compd* 2017;699:775–82.
- Zhang J, Li J, Chen G, Liu L, Chen Z, Meng Q, et al. Fabrication and characterization of a novel β metastable Ti-Mo-Zr alloy with large ductility and improved yield strength. *Mater Char* 2018;139:421–7.
- Zhang J, Sun F, Chen Z, Yang Y, Shen B, Li J, et al. Strong and ductile beta Ti-18Zr-13Mo alloy with multimodal twinning. *Materials Research Letters* 2019;7(6):251–7.
- Zhang J, Fu Y, Wu Y, Qian B, Chen Z, Inoue A, et al. Hierarchical $\{332\}$ - $\{113\}$ twinning in a metastable β Ti-alloy

- showing tolerance to strain localization. *Materials Research Letters* 2020;8(7):247–53.
- [30] Qian B, Liliensten L, Zhang J, Yang M, Sun F, Vermaut P, et al. On the transformation pathways in TRIP/TWIP Ti–12Mo alloy. *Mater Sci Eng, A* 2021;822.
- [31] Biesiekierski A, Ping D, Li Y, Lin J, Munir KS, Yamabe-Mitarai Y, et al. Extraordinary high strength Ti-Zr-Ta alloys through nanoscaled, dual-cubic spinodal reinforcement. *Acta Biomater* 2017;53:549–58.
- [32] Kuroda PAB, Buzalaf MAR, Grandini CR. Effect of molybdenum on structure, microstructure and mechanical properties of biomedical Ti-20Zr-Mo alloys. *Mater Sci Eng C Mater Biol Appl* 2016;67:511–5.
- [33] Ho W-F, Cheng C-H, Pan C-H, Wu S-C, Hsu H-C. Structure, mechanical properties and grindability of dental Ti–10Zr–X alloys. *Mater Sci Eng C* 2009;29(1):36–43.
- [34] Ji PF, Li B, Liu SG, Zhang X, Chen BH, Zhang XY, et al. Controlling the corrosion behavior of Ti-Zr alloy by tuning the α/β phase volume fraction and morphology of β phase. *J Alloys Compd* 2020;825.
- [35] Correa DRN, Kuroda PAB, Lourenco ML, Fernandes CJC, Buzalaf MAR, Zambuzzi WF, et al. Development of Ti-15Zr-Mo alloys for applying as implantable biomedical devices. *J Alloys Compd* 2018;749:163–71.
- [36] Zhao C, Zhang X, Cao P. Mechanical and electrochemical characterization of Ti–12Mo–5Zr alloy for biomedical application. *J Alloys Compd* 2011;509(32):8235–8.
- [37] Correa DRN, Vicente FB, Araujo RO, Lourenco ML, Kuroda PAB, Buzalaf MAR, et al. Effect of the substitutional elements on the microstructure of the Ti-15Mo-Zr and Ti-15Zr-Mo systems alloys. *J Mater Res Technol* 2015;4(2):180–5.
- [38] Sidhu SS, Singh H, Gepreel MAH. A review on alloy design, biological response, and strengthening of beta-titanium alloys as biomaterials. *Mat Sci Eng C-Mater* 2021;121.
- [39] Guo ZG, Ma TJ, Yang XW, Chen X, Tao J, Li J, et al. Linear friction welding of Ti60 near-alpha titanium alloy: investigating phase transformations and dynamic recrystallization mechanisms. *Mater Char* 2022;194.
- [40] N M. Mechanical properties of biomedical titanium alloys. *Mater Sci Eng, A* 1998;243(1–2):231–6.
- [41] Cordeiro JM, Beline T, Ribeiro ALR, Rangel EC, da Cruz NC, Landers R, et al. Development of binary and ternary titanium alloys for dental implants. *Dent Mater* 2017;33(11):1244–57.
- [42] Kuroda PAB, Lourenço ML, Correa DRN, Grandini CR. Thermomechanical treatments influence on the phase composition, microstructure, and selected mechanical properties of Ti–20Zr–Mo alloys system for biomedical applications. *J Alloys Compd* 2020;812:152108.
- [43] Oliveira NT, Biaggio SR, Rocha-Filho RC, Bocchi N. Electrochemical studies on zirconium and its biocompatible alloys Ti-50Zr at.% and Zr-2.5Nb wt.% in simulated physiologic media. *J Biomed Mater Res* 2005;74(3):397–407.
- [44] Xia C, Zhang Z, Feng Z, Pan B, Zhang X, Ma M, et al. Effect of zirconium content on the microstructure and corrosion behavior of Ti-6Al-4V- x Zr alloys. *Corrosion Sci* 2016;112:687–95.
- [45] Liu H, Yang J, Zhao X, Sheng Y, Li W, Chang C-L, et al. Microstructure, mechanical properties and corrosion behaviors of biomedical Ti-Zr-Mo-xMn alloys for dental application. *Corrosion Sci* 2019;161:108195.
- [46] Albrektsson T, Johansson C. Osteoinduction, osteoconduction and osseointegration. *Eur Spine J* 2001;10(Suppl 2):S96–101.